

This Page Is Inserted by IFW Operations
and is not a part of the Official Record

BEST AVAILABLE IMAGES

Defective images within this document are accurate representations of the original documents submitted by the applicant.

Defects in the images may include (but are not limited to):

- BLACK BORDERS
- TEXT CUT OFF AT TOP, BOTTOM OR SIDES
- FADED TEXT
- ILLEGIBLE TEXT
- SKEWED/SLANTED IMAGES
- COLORED PHOTOS
- BLACK OR VERY BLACK AND WHITE DARK PHOTOS
- GRAY SCALE DOCUMENTS

IMAGES ARE BEST AVAILABLE COPY.

**As rescanning documents *will not* correct images,
please do not report the images to the
Image Problem Mailbox.**

REMARKS

The Official Action dated February 6, 2004 has been received and its contents carefully noted. In view thereof, independent claim 6 has been amended in order to better define that which Applicants regard as the invention. Accordingly, claims 1-10, 12-15 and 21-24 are presently pending in the instant application with claims 1-5 being withdrawn from further consideration by the Examiner.

Referring now to the Official Action and particularly page 2 thereof, claims 6-10, 12-14 and 21-24 have been rejected under 35 U.S.C. §103 as being unpatentable over G.G. Shahidi et al., *High-Performance Devices for a 0.15 μ m CMOS Technology*, in view of U.S. Patent No. 5,923,987 issued to Burr. This rejection is respectfully traversed in that the combination proposed by the Examiner neither discloses nor remotely suggests that which is presently set forth by Applicants' claimed invention.

Initially, it is noted that with the foregoing amendments independent claim 6 recites a method for fabricating a semiconductor device including the steps of forming a gate electrode over a semiconductor region with the gate insulating film interposed therebetween, implanting heavy ions into the semiconductor region on both sides of the gate electrode using the gate electrode as a mask, implanting ions of a first dopant into the semiconductor region in which the amorphous layer has been formed using the gate electrode as a mask and conducting a first annealing process to activate the first and second ion implanted layers thereby forming an extended high concentration dopant diffused the layer of the first conductivity type through diffusion of the first dopant and a pocket dopant diffused layer of the second conductive type which is in contact with a bottom portion of the extended high concentration dopant diffused layer through diffusion of the heavy ions, wherein a dislocation loop layer is formed in the lower region of the amorphous layer in the semiconductor region

in the second step due to the heavy ion implantation and wherein the pocket dopant diffused layer is formed in the fourth step having a peaked dopant concentration produced by trapping heavy ions in the dislocation loop layer, the pocket dopant diffused layer and the extended high concentration dopant diffused layer being in contact at the peak dopant concentration of the pocket dopant diffused layer, and a side of the extended high concentration dopant diffused layer, located below the gate electrode, is not covered by the pocket dopant diffused layer.

That is, as the Examiner can readily appreciate from independent claim 6, the pocket dopant diffused layer is formed having a peak dopant concentration produced by trapping heavy ions in the dislocation loop layer. Further, the pocket dopant diffused layer and the extended high concentration dopant diffused layer are in contact at the peak dopant concentration of the pocket dopant diffused layer and a side surface of the extended high concentration dopant diffused layer, located below the gate electrode, is not covered by the pocket dopant diffused layer. It is respectfully submitted that the combination proposed by the Examiner fails to disclose or remotely suggest these features.

With reference being made to Fig. 1(b) of the Shahidi et al. reference, and we assume that the dopant profile shown therein illustrates a state immediately after ion implantation of the source-drain extension/halo as it appears the Examiner is suggesting, then it is clear that the Shahidi et al. reference fails to disclose a dopant profile after thermal treatment. As the Examiner can appreciate, in the dopant profile shown in Fig. 1(b) of Shahidi et al., the peak at a portion of the tail of the In concentration profile are in contact with the tail of the As concentration profile. Hence, if the amorphous layer of Shahidi et al. by implanting In ions such as that of the present invention, as shown in Fig. A attached hereinto, the amorphous/crystalline interface will be located deeper than the peak of the In concentration

profile. In this state, if the dislocation loop layer is formed by a thermal treatment as with the present invention, as shown in Fig. B attached hereto, the dislocation loop layer will be formed in a location deeper than the amorphous/crystalline interface, and the In concentration peak will be produced in the dislocation loop layer which is located deeper than the amorphous/crystalline interface by trapping In ions.

Consequently, according to Shahidi et al., the location at which the As diffusion layer and the In diffusion layer come in contact is not at the In concentration peak as set forth in accordance with Applicants' claimed invention. Thus Shahidi et al. is clearly different from the present invention and fails to disclose such invention. Further, Shahidi et al. fails to disclose forming a cross-sectional structure of the MOS transistor. Hence, Shahidi et al. fails to teach or suggest a side surface of the extended high concentration dopant diffused layer located below the gate electrode as not being covered by the pocket dopant diffused layer as is specifically recited by Applicants' claimed invention.

With reference to the teachings of Burr, according to the dosage of the pocket region ($5 \times 10^{11} - 1 \times 10^{13} /cm^2$), an amorphous layer would not be formed (naturally, segregation unique to indium also will not occur) regardless whether indium or boron is being used as the dopant. It is noted that the Examiner asserts since the dosage ($1 \times 10^{13} /cm^2$) in Burr is within the order of magnitude of the dose $5 \times 10^{13} cm^2$ for the present invention and an amorphous layer would be formed. However, as the Examiner can appreciate from the following discussion, this is not true. That is, for example, as can be clearly seen in Fig. 1 of the attached reference to G. Lulli et al. entitled *Structural Characterization and Modeling of Damage Accumulation of In Implanted Si*, from the Journal of Applied Physics, Volume 95, Number 1 dated January 1, 2004, under a dosage between a $1 \times 10^{13} cm^2$ and $3 \times 10^{13} /cm^2$ small defects are formed but an amorphous layer is not formed.

As shown in Fig. 5I of Burr, the pocket region 347 is formed covering the bottom and a side, that is the side located below the gate electrode 342 of the end-type source region 336A which functions as an extension region. Hence, Burr is readily distinguished from the present invention in which the side surface of the extended high concentration dopant diffused layer, located below the gate electrode, it is not covered by the pocket dopant diffused layer as recited in independent claim 6.

Accordingly, as noted hereinabove, both Shahidi et al. and Burr fail to disclose features which are specifically recited in independent claim 6. Particularly, each of these references when taken alone or in combination fail to disclose that the pocket dopant diffused layer and the extended high-concentration dopant diffused layer are in contact at the peak dopant concentration of the pocket dopant diffused layer and that a side surface of the extended high concentration dopant diffused layer located below the gate electrode, is not covered by the pocket dopant diffused layer. Consequently, it is respectfully submitted that Applicants' claimed invention as set forth in independent claim 6 as well as those claims which depend therefrom clearly distinguish over the combination proposed by the Examiner and are in proper condition for allowance.

With respect to paragraph 3 of the Office Action, claim 15 has been rejected under 35 U.S.C. §103(a) as being unpatentable over Shahidi et al. and Burr as applied to claim 6 above and further in view of U.S. Patent No. 5,399,506 issued Tsukamoto. This rejection is likewise respectfully traversed in that the patent to Tsukamoto fails to overcome the aforementioned shortcomings associated with the combination of Shahidi et al. and Burr.

While the patent to Tsukamoto may teach that RTA processes are well known in the art, it is respectfully submitted that Tsukamoto fails to overcome the significant shortcomings associated with the combination proposed by the Examiner as discussed in detail

hereinabove. Accordingly, it is respectfully submitted that Applicants' claimed invention as set forth in dependent claim 15 which includes all of the limitations of independent claim 6 clearly distinguishes over the combination proposed by the Examiner.

Therefore, it is respectfully requested that the rejections of record be reconsidered and withdrawn by the Examiner, that claims 6-10, 12-15 and 21-24 be allowed and that the application be passed to issue.

Should the Examiner believe a conference would be of benefit in expediting the prosecution of the instant application, he is hereby invited to telephone counsel to arrange such a conference.

Respectfully submitted,



Donald R. Studebaker
Reg. No. 32,815

Nixon Peabody LLP
401 9th Street N.W.
Suite 900
Washington, D. C. 20004
(202) 585-8000

Structural characterization and modeling of damage accumulation in In implanted Si

G. Lulli,^{a)} M. Bianconi, and A. Parisini

CNR—Istituto per la Microelettronica e i Microsistemi, Sezione di Bologna, Via P.Gobetti 101, I-40129 Bologna, Italy

E. Napolitani

INFN and Dipartimento di Fisica G. Galilei, Università degli Studi di Padova, Via Marzolo 8, I-35131 Padova, Italy

(Received 19 May 2003; accepted 15 October 2003)

Lattice disorder and dopant distribution in silicon implanted at room temperature with In ions have been characterized by cross-sectional transmission electron microscopy (XTEM), Rutherford backscattering channeling, and secondary ion mass spectroscopy techniques. It is shown that full recoil Monte Carlo calculation in the binary collision approximation, including an empirical damage efficiency parameter varying with ion dose, can reasonably reproduce the disorder distributions extracted from ion-channeling spectra, under the assumption of defects as atoms randomly placed in a rigid lattice. The main features of the observed trend, such as, for instance, the threshold for amorphization and the width of the amorphized layer, are in good agreement with XTEM observations. Furthermore, the good agreement between calculated and experimental as-implanted In distributions shows that the dynamic evolution of dopant profiles is consistent with the simulated damage growth. The distributions of displaced atoms extracted from ion channeling spectra and the depth profiles of measured contrast on XTEM images show different trends as a function of ion dose, which are attributed to the different sensitivity of the two techniques to the structural properties of ion damage and to the evolution of defects with increasing dose. The approximations used for the damage model employed for the simulation of ion channeling measurements are strictly related to the interpretation of disorder. Such relationships are pointed out and discussed on the basis of some discrepancies observed in the fitting of backscattering spectra. © 2004 American Institute of Physics. [DOI: 10.1063/1.1631076]

I. INTRODUCTION

Ion implantation of indium can be used to obtain ultrashallow and retrograde impurity profiles in Si. This process has been shown to improve near-surface channel mobility and reduce short-channel effects in submicron *p*-type channel metal-oxide-semiconductor field-effect transistors (nMOSFETs).^{1,2} Due to its heavy mass, In, even at the relatively low doses typically needed for channel doping, introduces a substantial amount of lattice disorder, which is expected to influence both the kinetics of dopant redistribution during subsequent thermal processes and the electrical characteristics of the final device. In recent years, transient enhanced diffusion (TED) effects^{3–8} and degradation of the electrical characteristics of nMOSFETs, due to defects produced by In channel implant,⁹ have been investigated. Because of the technological interest in the process, there have been some efforts to characterize damage accumulation¹⁰ and to develop predictive models for the simulation of In implantation in Si.^{11,12} A consistent model of this process should reproduce both dopant and disorder distribution profiles in the dose range of interest. Due to the low electrical activation of In in Si, and to the increasing doping densities required by deep submicron devices, the use of higher In doses is fore-

seen in the near future.⁹ It is therefore of interest to predict with good accuracy damage accumulation in the intermediate dose range, including cases of formation and growth of an amorphous layer.

In the present work, we investigate the process of damage accumulation in In implanted Si by transmission electron microscopy (XTEM) and Rutherford backscattering channeling (RBSC), while secondary ion mass spectroscopy (SIMS) is used for measuring as-implanted distribution profiles. The aim of this work is twofold. First, by comparing simulated and experimental dopant and disorder profiles, we aim to determine suitable parameters for predictive simulation of In implantation in Si by the Monte Carlo binary collision approximation (MC-BCA). Second, through a comparison of depth profiles of displaced atoms obtained by RBSC and of contrast extracted from XTEM micrographs, and a critical analysis of the procedure used to extract disorder profiles from RBSC spectra, we discuss some issues concerning the interpretation of structural measurements in ion implanted Si.

II. EXPERIMENT

(100) bare Si wafers (native oxide layer ~20 Å thick) were implanted at room temperature with 150 keV In ions at doses in the range 10^{12} – 10^{15} cm^{−2} under random alignment

^{a)}Electronic address: lulli@lamel.bo.cnr.it

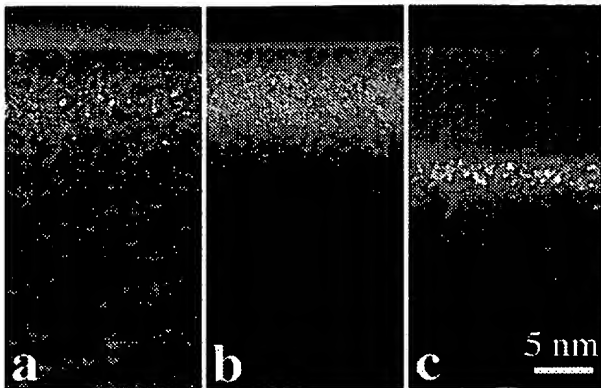


FIG. 1. Weak-beam dark field XTEM micrographs of the samples implanted at doses of (a) 10^{13} , (b) 3×10^{13} , and (c) 10^{14} In cm^{-2} . These micrographs have been obtained under identical WBDF settings, i.e., $g = \langle 400 \rangle$ ($-g, g$).

conditions, corresponding to a wafer tilt of 8° towards the $\langle 110 \rangle$ direction followed by a 22° rotation around the surface normal. Low ion dose rate was used in order to prevent any significant wafer heating during implantation.

XTEM observations were performed with a F.E.I. Tecnai F20 electron microscope operating at 200 kV. The microscope was equipped with a Gatan 794 Multiple Scan Camera (MSC) allowing digital image recording on a 1024×1024 pixels CCD array.

RBSC measurements were performed using 2 MeV He^+ particles aligned along the $\langle 001 \rangle$ Si axis, and a backscattering angle of 170° . More details on the experimental setup can be found elsewhere.¹³

As-implanted profiles were measured by SIMS with a CAMECA IMS-4f instrument using a 300 nA, 5.5 keV O_2^+ beam rastered over an area of $250 \times 250 \mu\text{m}^2$, while collecting $^{115}\text{In}^+$ ions from a small central area of 15 or $30 \mu\text{m}$ diameter in order to avoid border effects. The depth scale was calibrated under the assumption of constant sputtering rate by measuring the crater depth with a TENCOR P10 profilometer with a precision better than 1%. The concentration was calibrated by measuring an implantation standard with a dose known with an accuracy of 10%.

III. RESULTS

A. XTEM characterization and contrast depth profiles of implantation-induced defects

Cross-sectional weak-beam dark-field (WBDF) TEM investigations of the samples were performed for implantation doses ranging from 3×10^{12} to 10^{14} In cm^{-2} . As a first remark, these observations have shown the existence of a threshold dose for the visibility of the implantation-induced defects. In fact, no defects were detected in WBDF observations of 3×10^{12} In cm^{-2} implanted samples, whereas a damaged surface region extending in depth up to about $0.1 \mu\text{m}$ has been clearly observed at the higher In doses. In Figs. 1(a) and 1(b), the damaged surface layer consists of a band of small defects whose density appears to increase with increasing implantation dose. At the highest implantation dose,

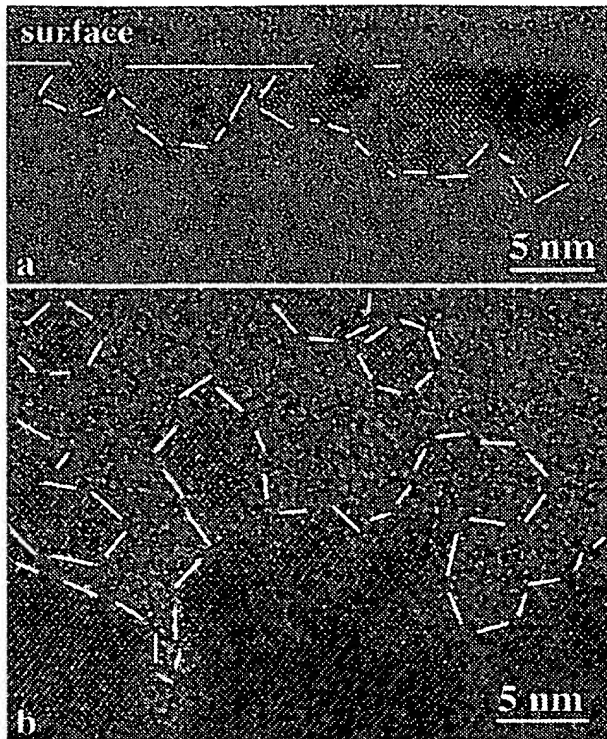


FIG. 2. High-resolution XTEM micrographs of (a) the surface region and (b) the deep amorphous-crystalline interface region of the sample implanted at a dose of 10^{14} In cm^{-2} [Fig. 1(c)]. White dashed lines are drawn as a guide to the eye to separate amorphous and crystalline regions.

this gives rise to the formation of an amorphous layer that is visible in Fig. 1(c) as a surface region of low intensity and uniform contrast. In this micrograph, residual bright contrast is observed in a very thin layer at the sample surface and at the interface between the amorphous region and the silicon bulk. The nature of these features is revealed in the high-resolution electron microscopy (HREM) micrographs reported in Figs. 2(a) and 2(b), respectively. In Fig. 2(a), a residual noncontinuous crystalline layer is observed at the sample surface extending in depth for a few nm. The presence of this layer, confirmed by the RBSC results shown in Fig. 6 of the next section, suggests that amorphization first occurred at the maximum defect distribution, which, for 150 keV In ions, falls at the depth of 40 nm, and subsequently extended both in-depth and toward the surface. The dose of 10^{14} In cm^{-2} is not sufficient for the amorphous layer to reach the surface. The occurrence of a continuous buried amorphous layer with residual crystalline material at the surface may prevent good recrystallization of the implanted layer upon subsequent thermal treatment, and should therefore be accurately controlled.

In Fig. 2(b), the transition region from the amorphous layer to the crystalline substrate is observed to be composed by crystalline islands embedded in the amorphous layer, followed by a heavily damaged crystalline substrate. This damaged crystalline region is visible in Fig. 1(c) as a layer of

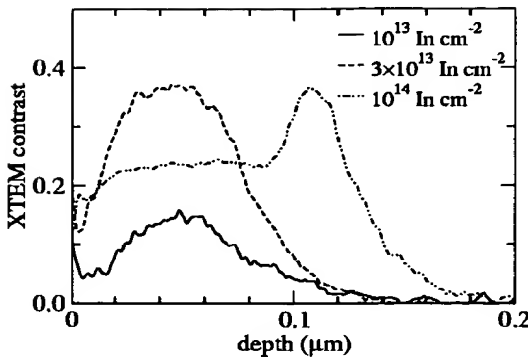


FIG. 3. Contrast depth profiles (units defined in Ref. 17) extracted by WBDF XTEM micrographs reported in Fig. 1.

bright contrast centered at a depth of about 110 nm. This is the well known end-of-range damage,¹⁴ which gives origin to $\{11\bar{3}\}$ defects and dislocation loops after annealing at moderate temperature.¹⁵ Following a procedure similar to that originally reported for the case of ion implanted SiC,¹⁶ and whose details are described in a previous work,¹⁷ depth profiles of contrast have been extracted from digitally recorded micrographs taken, in this case, under an identical WBDF setting, i.e., $g = \langle 400 \rangle (-g, g)$, thus extending this technique to the case of a varying implantation dose. Contrast depth profiles are defined as line profiles (averaged over a sufficiently wide image portion) of the quantity $C_a = (I_a - I_b)/(I_a + I_b)$, where I_a is the image intensity at pixel coordinates (i, j) and I_b represents a constant background intensity value.¹⁷ It is worthwhile to note that in this case, where TEM observations have to be performed on different samples, identical WBDF settings, i.e., $g = \langle 400 \rangle (-g, g)$, have been employed and that under these conditions the contrast, when measured in flat sample regions, was found to be substantially independent of the sample region thickness.

The extracted profiles corresponding to the implantation doses of Fig. 1 are reported in Fig. 3. As shown in this figure, in the case of implantation doses below the amorphization threshold, the contrast profiles exhibit a broad peak centered at a depth of about 50 nm from the sample surface. In this case, the increase of the XTEM contrast with the implantation dose appears to be slightly sublinear. However, it is worthwhile to remind the reader that in WBDF micrographs, contrast essentially measures the local deformation field around extended defects since it is only in these regions that the lattice planes are sufficiently distorted to be tilted back to the Bragg position.¹⁸ Thus coalescence of disordered regions or even the formation of amorphous islands may lead to an overall decrease of the contrast, i.e., integrals of contrast depth profiles based on WBDF micrographs are not, in general, proportional to the implantation dose or to the total implantation damage. This is particularly evident in the case of the dose of 10^{14} In cm^{-2} reported in Fig. 3, where the contrast of the amorphous region is observed to be lower than that of the disordered crystal below the $a-c$ interface [see also Figs. 1(c) and 2(b)]. From the XTEM contrast depth profile of this sample, it is possible to identify an av-

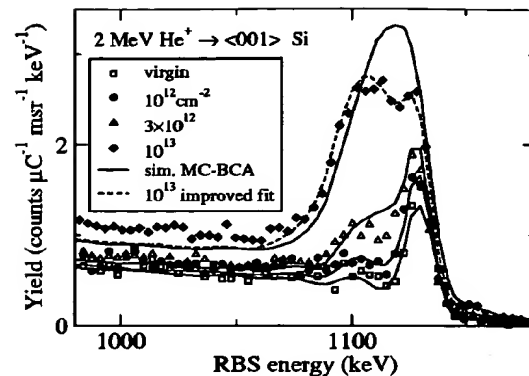


FIG. 4. RBSC spectra of samples implanted at low doses. Continuous lines are spectra simulations taking as input the disorder profiles shown in Fig. 6, calculated by full recoil MC-BCA simulations. The simulated spectrum indicated by the dashed line is the result of the improved fit for the sample implanted at 10^{13} In cm^{-2} (see the corresponding disorder profile reported Fig. 6).

erage position for the $a-c$ interface in the region where the contrast increases from the plateau characteristic of the continuous amorphous region to the peak in the underlying damaged crystalline layer.

B. RBSC characterization and MC-BCA simulation of disorder profiles

Figures 4 and 5 show experimental RBSC spectra of the samples implanted at low and medium-high doses, respectively. To extract disorder profiles from RBSC measurements, full simulation of the spectra is performed using the computer code BISIC.^{13,19} The disorder profiles used as a first trial input for spectra simulation are calculated with the full-recoil MC-BCA ion implantation code KING_99.^{20,21} It is known that, due to the influence of collective lattice response effects, the MC-BCA method underestimates the disorder produced by heavy ions, as shown by experiments,²² and molecular-dynamics (MD) computer simulation studies.^{23,24} To take into account this effect, we introduce a damage effi-

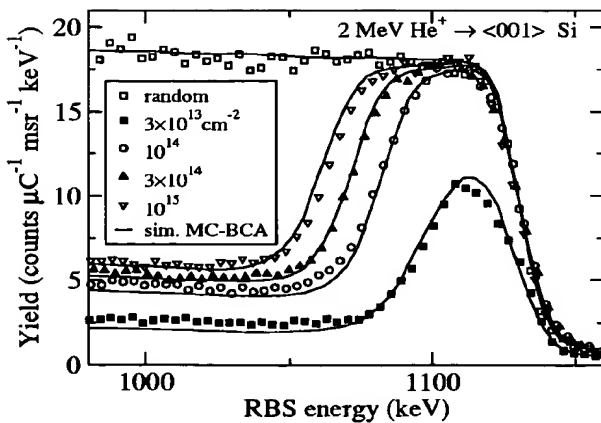


FIG. 5. The same of Fig. 4, for samples implanted at intermediate-high doses.

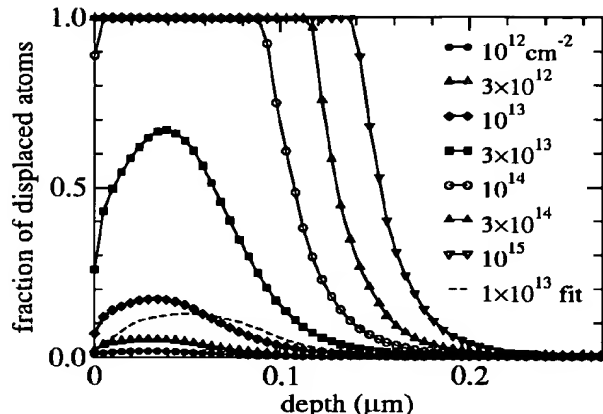


FIG. 6. Symbols connected by full lines indicate distribution profiles of displaced atoms calculated by MC-BCA, used as input to simulate the RBSC spectra reported in Figs. 4 and 5. For the dose of 10^{13} In cm^{-2} , the profile modified to improve the fitting of the RBSC spectrum as shown in Fig. 4 has been reported (dashed line) for comparison.

ciency parameter $\nu > 1$, conceptually similar to the one used in the Kinchin-Pease (KP) approximation.²⁵ We perform standard BCA full-recoil calculations using values of the threshold energy of atomic displacement E_d and of binding energy E_b typical of the pure binary collision regime, i.e., 13 and 1 eV, respectively.^{26,27} The point defect concentration produced by each ion, representative of a certain fraction of the total dose in the simulation, is calculated with the standard parameters E_d and E_b , multiplied by the empirical factor ν , and added to the defect concentration left by previous ions. The loss of crystal order with increasing dose is taken into account assuming that each atom which collides with the ion has a probability of being displaced from its lattice site equal to the local atomic concentration of defects. Damaged target atoms are assumed to be displaced at random in the lattice (random defect model). This assumption has been shown to predict the dechanneling effect of damage similar to the model of point defects as split- $\langle 110 \rangle$ interstitials.²⁸

To reproduce nonlinear behavior in damage growth, ν can be allowed to vary as a function of the implantation dose. The trend of ν versus dose is chosen to give profiles of displaced atoms which, when used as an input in the RBSC simulator BISIC, give the best overall fit of the experimental spectra in the whole range of implantation doses investigated.

Simulations in Figs. 4 and 5 are obtained with the disorder profiles shown in Fig. 6 as input. These profiles are the result of full-recoil MC-BCA simulations, using ν as reported in Fig. 7. The trend is indicative of a superlinear damage growth. A reasonably good agreement between the prediction of MC-BCA and the results of RBSC analysis is observed. It is worthwhile to note that for the dose of 10^{14} In cm^{-2} , the predictions of MC-BCA on the position of the deep α - c interface and on the presence of a thin residual damaged crystalline layer at the surface are in good agreement with XTEM observations. It is of interest to use the experimental data on the depth positions of the α - c interface at the three highest doses (deduced from Fig. 6) and the

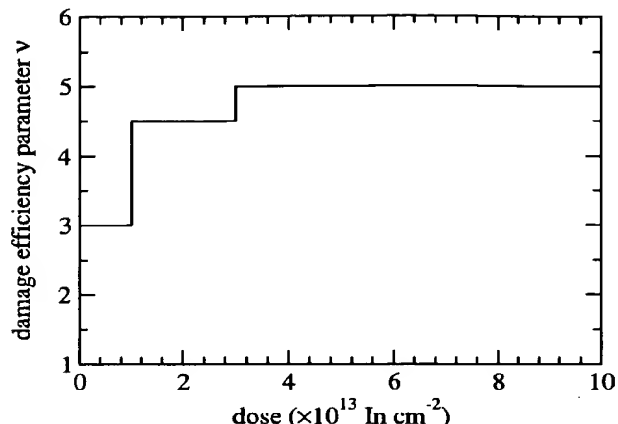


FIG. 7. Values of the damage efficiency parameter ν as a function of In dose, used to obtain the disorder profiles (Fig. 6) which give the best overall fit of RBSC spectra of Figs. 4 and 5.

calculated defect concentration at the same depths to evaluate the critical point defect density (CPDD) for amorphization. Using our own simulation code with standard E_d and E_b and setting the efficiency parameter ν equal to 1 to calculate defect concentration, we obtained a CPDD of about 5×10^{21} cm^{-3} for all doses. This value is lower than those relative to lighter ions, recently reviewed in Ref. 29.

The largest discrepancy between simulated and experimental RBSC spectra is found for the dose of 10^{13} In cm^{-2} , where significant differences in both width and height of the damage peak are observed. Only for this particular case was the disorder profile adjusted to improve the poor fit of the damage peak given by MC-BCA. The resulting simulated spectrum is shown in Fig. 4, while the corresponding modified disorder profile is reported in Fig. 6, where it can be compared with the one calculated by MC-BCA.

C. SIMS analysis

In Fig. 8, experimental (SIMS) and simulated as-implanted In distribution profiles are compared for different implantation doses. For the calculation of In-Si elastic scattering, the universal Ziegler, Biersack, and Littmark (ZBL)³⁰ interatomic potential has been used. For the random electronic cross section we use values deduced by Ref. 30 (routine TRIMSTOP). It is worth noting that for 150 keV In implantation in Si, elastic nuclear collisions are the main mechanism of energy loss, and the details of the electronic energy-loss model have little influence on the calculated dopant profiles. Deep channeling tails in dopant distributions saturate with increasing dose due to the decreasing probability of channeling with increasing lattice damage. This behavior should be reproduced by a consistent modeling of damage accumulation. Actually, the good agreement observed between simulations and measurements indicates that the dynamic evolution of In profiles is consistent with the calculated damage accumulation. Some minor difference is observed for the highest dose (10^{15} In cm^{-2}), where the

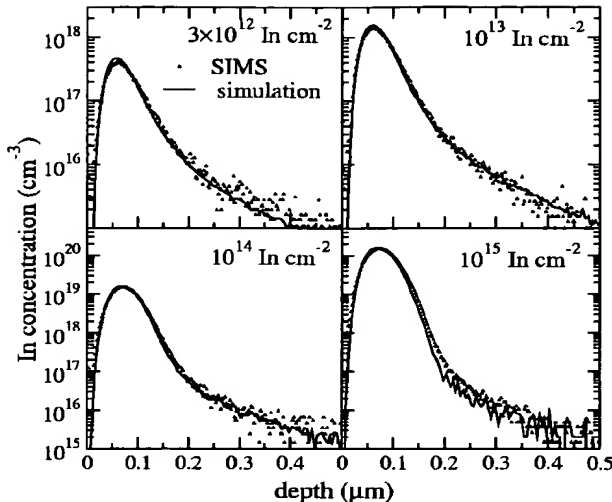


FIG. 8. Comparison between experimental SIMS depth-distribution profiles of as-implanted In, and profiles simulated by MC-BCA using the damage efficiency parameter as reported in Fig. 7.

calculation overestimates the dechanneling effect of disorder on In ions, giving a channeling tail slightly less pronounced than its experimental counterpart.

IV. DISCUSSION

Results of RBSC and SIMS characterization have shown that MC-BCA simulation can reproduce the essential features of the ion implantation process of In in Si. However, some discrepancies have been observed in the comparison between simulated and experimental RBSC spectra, in particular for the case of the sample implanted at 10^{13} In cm^{-2} . Moreover, we observe that the simulations (Figs. 4 and 5) systematically underestimate the experimental spectra in the region below the damage peak.

In Fig. 9, RBSC disorder depth profiles and XTEM contrast depth profiles are compared. For the dose of 10^{13} In cm^{-2} , the profile adjusted to better fit the RBSC spectrum has been used for the comparison. In Fig. 9(a), a qualitative agreement between MC-BCA and XTEM profiles is observed. The XTEM contrast profile of the sample implanted at the dose of 3×10^{13} In cm^{-2} is slightly shifted in depth in comparison with the MC-BCA profile. For the purpose of comparison, XTEM contrast depth profiles have all been scaled by the same arbitrary factor. It is therefore clear that XTEM and MC-BCA damage profiles do not scale in a similar way with implantation dose. As mentioned in Sec. III A, the behavior of XTEM contrast is attributed to the fact that the lattice strain per interstitial decreases with increasing the size of the interstitial aggregates, until amorphous regions are formed. Also, the RBSC yield is sensitive to the lattice distortion induced by defects, but it is quantitatively more sensitive to the total amount of atoms displaced from regular lattice sites. In fact, the probability of backscattering of a channelled beam increases with increasing disorder, and saturates only when amorphization occurs. This gives a nearly monotonic increase of RBSC yield with increasing the

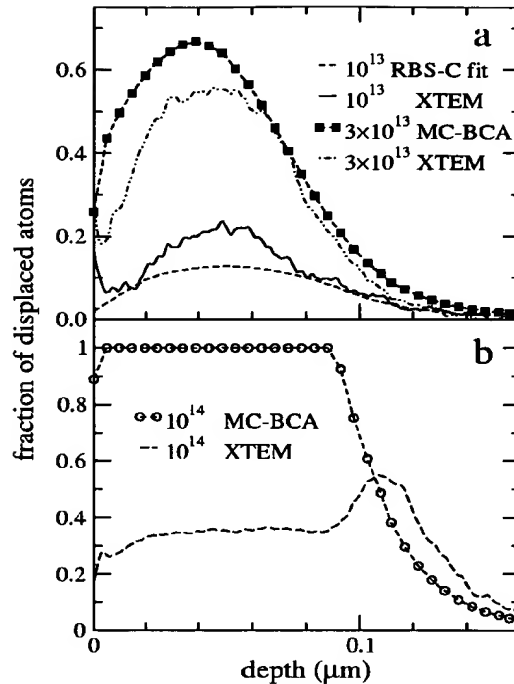


FIG. 9. Comparison of disorder profiles determined by RBSC analysis and profiles of contrast extracted from XTEM WBDF micrographs, for the doses of (a) 10^{13} and 3×10^{13} and (b) 10^{14} In cm^{-2} . Contrast profiles have been all scaled by the same constant factor to be compared with MC-BCA results. For the dose of 10^{13} In cm^{-2} the disorder profile adjusted to improve the fitting of RBSC spectrum has been reported.

total amount of disorder. Full simulation of RBSC spectra in target-containing defects is the most accurate method to estimate the distribution of displaced atoms, nevertheless we observe discrepancies in Figs. 4 and 5. This may be attributed to the simplified model of defects used in the simulation, i.e., atoms displaced randomly in a rigid lattice. As discussed in detail elsewhere^{17,31} the random defect model does not take into account the strain field associated with defects, and this is probably why it is difficult to fit both scattering yield and dechanneling simultaneously at low-intermediate doses, where damage is mostly in the form of point defects and small aggregates. It is worthwhile to note that in the limiting case where a fully amorphous layer terminated by an abrupt $a-c$ interface exists, as reported in Fig. 10 for the case of amorphous Si films (thickness in the range 12–255 nm) deposited on virgin (100) Si substrates,³² the dechanneling in the underlying crystal is perfectly reproduced by calculations.

V. CONCLUSIONS

The accumulation of disorder in room-temperature In implanted Si follows with reasonably good accuracy the predictions of full cascade MC-BCA modeling, assuming a value of the empirical damage coefficient ν increasing from 3 to 5 in the dose interval 10^{12} – 10^{14} In cm^{-2} . This setting enables a consistent modeling of In implantation in Si, which, under the assumption of the random defect model,

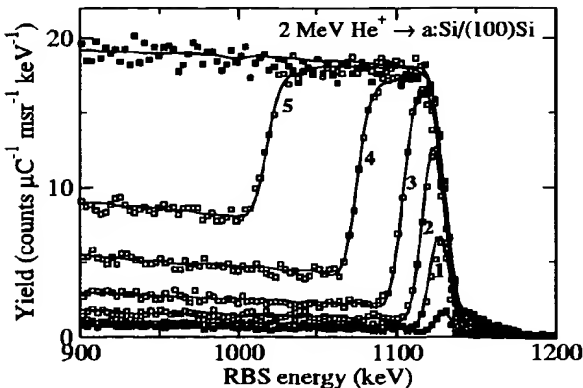


FIG. 10. RBSC spectra of a :Si/(100)Si samples (open squares) and of (100) virgin and random references (filled squares). Numbers refer to spectra from deposited a :Si layers of different thicknesses: (1) 12 nm, (2) 29 nm, (3) 60 nm, (4) 125 nm, (5) 255 nm. Continuous lines are simulations.

reproduces the essential features of the evolution of both disorder and impurity distribution profiles in the range of doses up to target amorphization. The comparison between depth profiles of displaced atoms extracted from RBSC and of XTEM contrast measured on WBDF micrographs points out that the quantitative analysis of disorder is dependent on the sensitivity of each structural technique to the properties of ion induced defects, properties which change with increasing implantation dose. In particular, lattice strain induced by defects influences the response of both techniques, but it has a stronger effect on the formation of XTEM contrast, since a large contribution to the RBSC yield comes from the direct scattering of channeled ions with displaced lattice atoms. However, the quantitative information on disorder profiles extracted from RBSC measurements may be affected by neglecting lattice strain, as actually occurs in the standard models used so far. For instance, the inability to account for the dechanneling induced by the strained lattice around defects can lead to the observed discrepancies in the fitting of RBSC spectra, most evident at low-intermediate doses where ion damage consists of a partially disordered crystal. As expected, these discrepancies become smaller at higher implantation doses, where lattice strain is reduced due to the formation of an amorphous layer.

We have seen that both XTEM contrast and RBSC yield are sensitive to the strain induced by defects in the lattice and that this sensitivity has consequences on the interpretation of results of both techniques. So far, there have been only a few attempts to introduce a consistent modeling of defects, including their deformation field, for the interpretation of RBSC experiments.^{31,33} The comparison of results of RBSC and of other structural techniques more specifically sensitive to lattice strain, such as XTEM and x-ray diffraction, can be helpful not only for a better understanding of the nature of implantation damage, but also as a support in the development of more physically based models of defects.

ACKNOWLEDGMENTS

Thanks are due to A. Bartolucci for XTEM specimen preparation and to R. Lotti for technical assistance in RBSC

measurements. This work was partially supported by the FIRB national project (Contract No. RBAU01LLX2).

- ¹G. G. Shahidi, B. Davari, T. J. Bucelot, P. A. Ronsheim, P. J. Coane, S. Pollack, C. R. Blair, B. Clark, and H. H. Hansen, IEEE Electron Device Lett. **14**, 409 (1993).
- ²S.-J. Chang, C.-Y. Chang, T.-S. Chao, and T.-Y. Huang, IEEE Electron Device Lett. **21**, 127 (2000).
- ³P. B. Griffin, M. Cao, P. Vande, Y.-L. Chang, and W. M. Greene, Appl. Phys. Lett. **73**, 2986 (1998).
- ⁴O. Dokumaci, P. Ronsheim, C. D'emic, A. G. Domenicucci, S. Hedge, P. Kozlowski, and H.-S. P. Wong, Mater. Res. Soc. Symp. Proc. **568**, 205 (1999).
- ⁵T. Noda, S. Odanaka, and H. Umimoto, J. Appl. Phys. **88**, 4980 (2000).
- ⁶T. Noda, J. Appl. Phys. **91**, 639 (2002).
- ⁷S. Solmi, A. Parisini, M. Bersani, D. Giubertoni, V. Soncini, G. Carnevale, A. Benvenuti, and A. Marmiroli, J. Appl. Phys. **92**, 1361 (2002).
- ⁸T. Noda, J. Appl. Phys. **93**, 1428 (2003).
- ⁹H. Liao, D. S. Ang, and C. H. Ling, IEEE Trans. Electron Devices **49**, 2254 (2003).
- ¹⁰G. Pavia, A. Losavio, A. Queirolo, G. Zanderigo, and F. Ottaviani, in *Proceedings of the 11th Conference on Microscopy of Semiconducting Materials*, edited by A. Cullis (Institute of Physics, Bristol, 1999), p. 469.
- ¹¹M. J. Rendon, P. Zeitoff, and S. Ravi, in *Proceedings of the 12th International Conference on Ion Implantation Technology*, edited by J. Matsuo, G. Takaoka, and I. Yamada (IEEE, Piscataway, NJ, 1998), p. 740.
- ¹²Y. Chen, B. Obradovich, B. Morris, and G. Wang, in *Proceedings of the 5th International Symposium on Process Physics and Modeling in Semiconductor Technology*, edited by C. S. Murthy (Electrochemical Society, Pennington, NJ, 1999), p. 33.
- ¹³G. Lulli, E. Albertazzi, M. Bianconi, G. G. Bentini, and R. Lotti, Nucl. Instrum. Methods Phys. Res. B **170**, 1 (2000).
- ¹⁴K. S. Jones, S. Prussin, and E. R. Weber, Appl. Phys. A: Solids Surf. **45**, 1 (1988).
- ¹⁵C. Bonafos, D. Mathiot, and A. Claverie, J. Appl. Phys. **83**, 3008 (1998).
- ¹⁶J. Grisolia, B. de Mauduit, J. Gimbert, T. Billon, G. B. Assayag, C. Bourgerette, and A. Claverie, Nucl. Instrum. Methods Phys. Res. B **147**, 62 (1999).
- ¹⁷G. Lulli, M. Bianconi, A. Parisini, S. Sama, and M. Servidori, J. Appl. Phys. **88**, 3993 (2000).
- ¹⁸C. J. Humphreys and R. A. Drummond, in *Electron Microscopy and Analysis 1977, Inst. Phys. Conf. Ser. No. 36* (Institute of Physics, Bristol, 1977), p. 241.
- ¹⁹E. Albertazzi, M. Bianconi, G. Lulli, R. Nipoti, and M. Cantiano, Nucl. Instrum. Methods Phys. Res. B **118**, 128 (1996).
- ²⁰E. Albertazzi, M. Bianconi, G. Lulli, R. Nipoti, A. Carnera, and C. Cellini, Nucl. Instrum. Methods Phys. Res. B **112**, 152 (1996).
- ²¹G. Lulli, E. Albertazzi, M. Bianconi, R. Nipoti, M. Cervera, A. Carnera, and C. Cellini, J. Appl. Phys. **82**, 5958 (1997).
- ²²D. A. Thompson and R. S. Walker, Radiat. Eff. **36**, 91 (1978).
- ²³M. J. Caturla, T. D. de la Rubia, L. A. Marques, and G. H. Gilmer, Phys. Rev. B **54**, 16 683 (1996).
- ²⁴K. Nordlund, M. Ghaly, R. S. Averback, M. Caturla, T. D. de la Rubia, and J. Tarus, Phys. Rev. B **57**, 7556 (1998).
- ²⁵G. H. Kinchin and R. S. Pease, Rep. Prog. Phys. **18**, 1 (1955).
- ²⁶J. W. Corbett and J. C. Bourgois, in *Point Defects in Solids Vol. 2*, edited by J. H. Crawford, Jr. and L. M. Sifakis (Plenum Press, New York, 1975).
- ²⁷M. Mazzarolo, L. Colombo, G. Lulli, and E. Albertazzi, Phys. Rev. B **63**, 195207 (2001).
- ²⁸G. Hobler, A. Simionescu, L. Palmethofer, F. Jahn, R. von Criegern, C. Tian, and G. Stinger, J. Vac. Sci. Technol. B **14**, 272 (1996).
- ²⁹G. Hobler and G. Otto, Nucl. Instrum. Methods Phys. Res. B **206**, 81 (2003).
- ³⁰J. F. Ziegler, J. P. Biersack, and U. Littmark, *The Stopping and Range of Ions in Solids* (Pergamon, New York, 1985).
- ³¹S. Balboni, E. Albertazzi, M. Bianconi, and G. Lulli, Phys. Rev. B **66**, 045202 (2002).
- ³²M. Bianconi, R. Nipoti, M. Cantiano, A. Gasparotto, and A. Sambo, Nucl. Instrum. Methods Phys. Res. B **84**, 507 (1994).
- ³³B. Weber, E. Wender, K. Gärtner, D. M. Stock, and W. Wesch, Nucl. Instrum. Methods Phys. Res. B **118**, 113 (1996).